Journal of Materials Chemistry A

PAPER

View Article Online
View Journal | View Issue

Cite this: J. Mater. Chem. A, 2017, 5, 7394

Design of coherent anode materials with 0D Ni_3S_2 nanoparticles self-assembled on 3D interconnected carbon networks for fast and reversible sodium storage†

Xu Zhao,[abc] Hong-En Wang,[c] Robert C. Massé,[c] Jian Cao,[a] Jiehe Sui,[ab] Jiangyu Li,[d] Wei Cai*[b] and Guozhong Cao*[c]

Received 2nd February 2017
Accepted 20th March 2017

DOI: 10.1039/c7ta01056g

rsc.li/materials-a

There has been tremendous progress in development of nanomaterials for energy conversion and storage, with sodium-ion batteries (SIBs) attracting attention because of the high abundance of raw materials and low cost. However, inferior cycling stability, sluggish reaction kinetics, and poor reversibility hinder their practical applications. In the present study, Ni_3S_2/carbon nanocomposites with coherent nanostructures were successfully used as anodes in half- and full-cells. Outstanding cycling and rate performances are attributed to a synergistic effect between the Ni_3S_2 nanoparticles and interconnected carbon networks. The coherent porous framework effectively alleviated volume changes of Ni_3S_2, shortened the Na^+ diffusion path, and accelerated electron transport and ionic diffusion during the electrochemical reaction. More importantly, conversion reaction products can be confined by the entangled carbon networks, leading to reversible redox reactions as demonstrated in *ex situ* XRD studies. The coherent Ni_3S_2/C nanocomposites demonstrated a highly reversible charge capacity of 453 and 430 mA h g^{-1} at a current density of 0.1 and 0.4 A g^{-1} over 100 cycles, respectively. At a current density of 2.0 A g^{-1}, high rate capacities of 408 mA h g^{-1} can be attained over 200 cycles. The high performance of $Na_3V_2(PO_4)_3/Ni_3S_2$ full-cells enrich prospects for future practical applications.

1. Introduction

The ever-increasing global consumption of fossil fuels and their consequent environmental pollution have become a pressing challenge in modern society.[1,2] A variety of clean renewable energy conversion and storage technologies have been investigated and some have been successfully commercialized, such as solar cells, supercapacitors, lithium ion batteries, and thermoelectric devices.[3–5] Intensive research and industrial development of lithium ion batteries (LIBs) over the past 30 years[6] have made them an indispensable portable power source, pervasive in our electronic device-dependent modern life, because of their high-energy density and environmental friendliness as well as long cyclic life. Despite the great success and steady advancement of LIB technology, there remain some challenges.[2,3] The relatively low abundance of Li has forced researchers to pursue alternative technologies with materials in higher abundance with broader distribution.[7–9] Sodium ion batteries (SIBs) are one of the most promising alternatives studied in recent years, as sodium is one of the most abundant elements on the Earth.[2,9–12] In addition, sodium shares similar structure and energy storage mechanism with its lithium counterpart. Hence, there is strong interest in developing high-performance anodes[13,14] and cathodes[15,16] for SIBs. As the sodium ion possesses a larger ionic radius than the lithium ion (1.02 Å *vs.* 0.76 Å),[3] electrodes commonly suffer from slow sodium ion diffusion and large pulverization during discharge/charge processes. Various nanostructured materials have been studied to circumvent the slow kinetics in development of new electrodes for SIBs. In addition to metal oxides, transition metal sulfides (MS_x) have been explored as alternative anodes in LIBs and SIBs because of their good mechanical stability and enhanced reversibility.[17–20] The weaker chemical bonding of M–S than that of M–O could also be favorable for the electrochemical processes.[18]

Nickel sulfides (NiS_x) including NiS, NiS_2, Ni_3S_2, and Ni_9S_8 are widely known as promising anode materials.[21–24] Among them, Ni_3S_2 exhibits some unique properties in various clean

[a]State Key Laboratory of Advanced Welding and Joining, Harbin Institute of Technology, Harbin 150001, China
[b]School of Materials Science and Engineering, Harbin Institute of Technology, Harbin, 150001, China. E-mail: weicai@hit.edu.cn
[c]Department of Materials Science and Engineering, University of Washington, Seattle, WA, 98195, USA. E-mail: gzcao@u.washington.edu
[d]Department of Mechanical Engineering, University of Washington, Seattle, WA 98195, USA

† Electronic supplementary information (ESI) available. See DOI: 10.1039/c7ta01056g

energy technologies, including photocatalytic and electrocatalytic production of H_2 and supercapacitors.[25–27] Ni_3S_2 has attracted attention as a promising anode in SIBs because of its stable forms and smaller volume change than other nickel sulfides.[28] Commonly known as a "Heazlewoodite"-type mineral,[29] it is naturally abundant, cheap, and stable. The overall reaction of Ni_3S_2 in SIBs is given in eqn (1):

$$Ni_3S_2 + 4Na^+ + 4e^- \leftrightarrow 3Ni + 2Na_2S \quad (1)$$

When used in SIB anodes, Ni_3S_2 suffers from poor electrical conductivity, large pulverization, and insufficient surface area for electrolyte contact.[28,29] Several strategies have been reported to improve the electrochemical properties through hybridizing Ni_3S_2 with conductive polymer,[30] carbon nanotube,[31] graphene,[32] and nickel foam.[33] However, despite some success, the SIB performances are still unsatisfactory because of the irreversible conversion reaction. This drawback is usually a result of multiple electron transfers occurring per metal centre during the conversion reactions,[19] making conversion of the Ni_3S_2 to metal Ni and Na_2S in the initial sodiation process irreversible. As a result, most of the Na_2S generated *in situ* cannot effectively react with the Ni to recover the Ni_3S_2 phase in the recharge process. The unreacted Na_2S can be oxidized to poly-sulfides during the desodiation process, which experience a dissolving/shuttle effect leading to severe capacity losses, as known in Li–S batteries.[10,19] Xie *et al.* introduced a protected carbon layer on the surface of $MoSe_2$ and CVD–graphene nanocomposites to suppress the "shuttle effect" resulting in a high performance SIB anode.[10] George *et al.* used "double wall carbon nanotubes (DWCNTs)" in the MoS_2 electrode to form an entangled network to migrate the shuttle effects, achieving promoted LIBs performance.[17] However, the high cost of preparation procedures and high-rate performances are still not ideal. Therefore, development of a Ni_3S_2 electrode with fast kinetics for high storage capacity at a high rate remains challenging.

From this perspective, this study demonstrates fast and reversible sodium ion storage in coherent Ni_3S_2/carbon nanocomposites (referred as Ni_3S_2/C). First, coherent carbon networks derived from NaCl as template and citric acid as carbon precursor, not only provide sufficient contacts between Ni_3S_2 and electrodes, but also shorten sodium-ion diffusion pathways and enhance electrical conductivities.[34–37] Moreover, the entangled confinement, coherent structure effectively promoted the reversible reaction by confining discharge products. The resulting unique interconnected structures demonstrated excellent cyclic and rate properties (retention 85% and 87% at 0.1 and 0.4 A g^{-1} for 100 cycles, respectively. 408 mA h g^{-1} at 2.0 A g^{-1} over 200 cycles). A $Na_3V_2(PO_4)_3$/rGO || Ni_3S_2/C full cell with excessive cathode materials was assembled and found to deliver a storage capacity of 101 mA h g^{-1} over 30 cycles at 0.5 A g^{-1}. Enhanced sodium ion diffusion and high reversibility lead to high-rate capacity and cyclic performance. The purposely designed coherent Ni_3S_2/C nanostructure exhibits higher reversible capacity and rate capability when used as an SIB anode compared with reported Ni_3S_2-based electrodes.

2. Experimental sections

2.1 Chemicals and materials

All chemicals were used without further purification. Nickel(II) nitrate hexahydrate ($Ni(NO_3)_2 \cdot 6H_2O$, 98%), sodium carbonate (Na_2CO_3, 98%), and sodium chloride (NaCl, 99.0%) were bought from Alfa Aesar, USA. Thiourea (CH_4N_2S, 99.0%), citric acid ($C_6H_8O_7$, 99%), ammonium dihydrogen phosphate ($NH_4H_2PO_4$, 99.999%), and vanadyl acetylacetonate ($V(acac)_3$, 98%) were purchased from Sigma-Aldrich, USA. Ultrapure deionized water was used for preparation of all aqueous solutions.

2.2 Synthesis of coherent Ni_3S_2/C nanocomposites

In a typical synthesis process, 0.29 g of $Ni(NO_3)_2 \cdot 6H_2O$ and 0.38 g of thiourea were dissolved in 20 mL deionized (DI) water with stirring at room temperature. Then 0.18 g of citric acid and 4 g NaCl were added, and stirred for 30 min. Then the mixture was frozen in a refrigerator at −20 °C overnight, followed by freeze-drying under vacuum for 48 h. The obtained gel was ground and further annealed under high-purity nitrogen (N_2) for 2 h at 800 °C with a ramping rate of 5 °C min^{-1}, then cooled to room temperature naturally under the protection of N_2. The obtained black powders were washed five times using DI water to completely remove the NaCl template. After drying in air at 45 °C for 12 h, the final products were obtained.

2.3 Synthesis of $Na_3V_2(PO_4)_3$ cathode material

$Na_3V_2(PO_4)_3$/graphene composites (named NVP/rGO) were synthesized as reported in the literature.[16] 0.75 mmol Na_2CO_3, 1 mmol $V(acac)_3$, and 1.5 mmol $NH_4H_2PO_4$ were dissolved in 30 mL DI water and stirred for 12 h at room temperature. NVP gel was obtained *via* a hydrothermal reaction at 180 °C for 6 h. Then 4.5 mL graphene oxide solution (prepared by modified Hummers' method, 2 mg mL^{-1}) was added with strong stirring. After freeze-drying, NVP/rGO precursors were obtained through heat treatment with the condition of Ar/H_2, 95 : 5 in vol% and 750 °C for 8 h.

2.4 Structural characterizations

Crystal structures of the samples were identified using X-ray diffraction (PANalytical X'Pert Pro with Cu-Kα radiation). The Raman spectrum was obtained using a Renishaw inVia system (Renishaw inVia Raman Microscope, the USA) with a laser wavelength of 514 nm. Thermogravimetric analysis (TGA) was performed on a TG instrument (NETZSCH STA 409 C) from room temperature to 700 °C in air with heating rate of 10 °C min^{-1}. Morphologies were characterized using a field emission scanning electron microscope (SEM, FEI Sirion XL30). Microstructures were investigated using a transmission electron microscope (TEM, FEI Tecnai G2 F20). XPS measurements were performed using an X-ray microprobe (Thermo Fisher Scientific ESCALAB 250Xi) with Al Kα radiation. Nitrogen adsorption–desorption isotherms were measured using a Quanta-chrome NOVA 4200e system. Specific surface areas were determined using a multi point-Brunauer–Emmett–Teller (BET) method.

2.5 Electrochemical measurements

Half cells were performed using coin-type 2016 cells at room temperature. The working electrode was prepared by mixing the active materials, carbon black (Super-P), and poly(vinyl-difluoride) (PVDF) at a weight ratio of 8 : 1 : 1, and then pasting on pure Cu foil, followed by drying at 80 °C under vacuum overnight. For the SIB half cell, sodium pieces were used as both the counter electrode and reference electrode, glass fiber (Whatman GF/A) as the separator, and 1 M $NaClO_4$ in ethylene carbonate/diethyl carbonate/fluoroethylene carbonate (EC/DEC/FEC, 1 : 1 : 0.05 in volume%) as electrolyte. For sodium full-cell testing, the cathode material was NVP/rGO and the battery was assembled in a standard CR2032-type coin cell. The specific capacity was calculated based on the mass of the anode-active material. Cell assembly was carried out in an argon-filled glovebox (M. Braun) with water and oxygen concentrations below 0.5 ppm. The fresh cells were aged for 12 h before the measurements to ensure full percolation of the electrolyte. Cyclic voltammetry (CV) curves were recorded on a CHI 605C electrochemical workstation (the scan rate was 0.2 mV s^{-1}). The galvanostatic charge–discharge tests were performed on a LAND CT-2100A battery tester. The voltage window was in the range of 0.01–3 V (*vs.* Na^+/Na). Electrochemical impedance spectroscopy (EIS, carried out on a Solartron 1260 instrument) was examined by applying an AC voltage of 5 mV over the frequency range from 0.01 Hz to 100 kHz. The volumetric capacities are based on the volume of whole anode with a thickness of about 100 μm, including active materials, carbon black and binder.

3. Results and discussions

3.1 Growth strategy and structure characterization of coherent Ni_3S_2/C

The coherent Ni_3S_2/C nanocomposite was synthesized *via* template-directed sol–gel processing and post-annealing, as illustrated in Fig. 1. First, precursor was prepared by dissolving $Ni(NO_3)_2$, thiourea, citric acid, and NaCl in DI water at room temperature to form a homogeneous solution. The solution was then frozen in a freezer for 24 hours at −20 °C. During this step, NaCl crystallizes to form small crystallites that serve as hard templates. Afterwards, water was removed *via* a freeze-drying process (−20 °C for 2 days). As shown in Fig. S1a,† NaCl cubic crystals with an average diameter of 10 microns were formed. Subsequent annealing treatment at 800 °C in high purity N_2 for 2 h resulted in black mixtures containing Ni_3S_2/C adsorbed on the surface of cubic NaCl (Fig. S1b†). Finally, coherent Ni_3S_2/C was obtained by dissolving NaCl in water (Fig. S1c†).

Fig. 2a presents the X-ray diffraction (XRD) pattern of coherent Ni_3S_2/C nanocomposite. All the diffraction peaks match well with crystalline Ni_3S_2 (JCPDS no. 44-1418) with peaks at 2θ of 21.7°, 31.1°, 37.8°, 44.3°, 49.7° and 55.1° readily assigned to respective (101), (110), (003), (202), (113), and (122) facets of Ni_3S_2. No other phases derived from other impurities could be detected, indicating the high phase purity of as-prepared samples. Fig. S2† shows phase purity of coherent Ni_3S_2/C composites before and after removal of NaCl as templates for pores. In addition to strong peaks of NaCl (JCPDS no. 87-0712), other peaks are in good accordance with Ni_3S_2 of Heazlewoodite phase. The influence of annealing temperature on phase purity is shown in Fig. S3.† At low annealing temperature (600 °C), a mixture of several nickel sulfides containing $Ni_{0.96}S$, Ni_9S_8, and Ni_3S_2 can be detected, which may be ascribed to insufficient reactions of the precursors. Increasing the temperature to 700 °C, the $Ni_{0.96}S$ disappeared and the main phases were indexed to Ni_3S_2 and Ni_9S_8. On increasing the temperature further to 800 °C, the as-obtained products were all pure Ni_3S_2 without other nickel sulfides. Results indicate that Ni_3S_2 is more stable than other nickel sulfides, which is helpful for practical applications. Thermogravimetric analyses (TGA) of "$Ni(NO_3)_2$ + thiourea + citric acid + NaCl" composites were conducted under N_2 from room temperature to 800 °C (Fig. S4a†), with a ramping rate of 5 °C min^{-1}. The initial weight losses (<300 °C) could be assigned to evaporation of crystal water and decomposition of Ni-salt. From 300 °C to 800 °C, together with results shown in Fig. S3,† continuous sulfurization processes occurred.

Fig. 2b shows scanning electron microscopy (SEM) images of the product before washing NaCl templates. Micro-sized cubic NaCl crystals are encapsulated uniformly in a thin film-like Ni_3S_2/C nanocomposite. As-mentioned self-assembly strategies

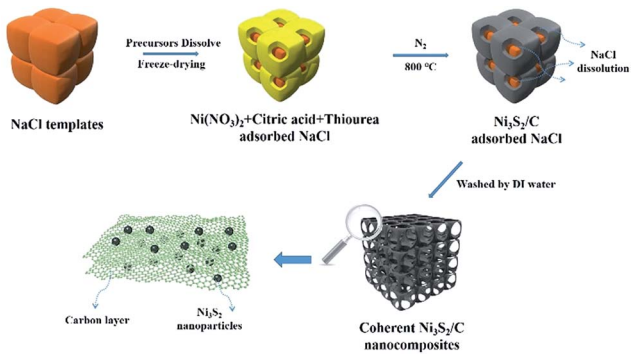

Fig. 1 Fabrication strategy of coherent Ni_3S_2/C nanocomposites using NaCl as template and citric acid as carbon source.

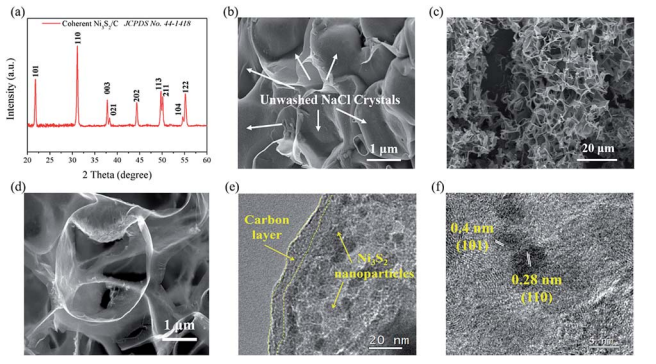

Fig. 2 (a) XRD pattern; SEM images of (b) before, (c) and (d) after removal of NaCl template, (e) and (f) TEM images of Ni_3S_2/C composites (scale bar is 20 nm and 5 nm).

provide a surface for directing synthesis of the Ni_3S_2/carbon networks. From the SEM image of Fig. 2c, the laminar Ni_3S_2/carbon foam-like structure with a 3D interconnected macro-porous network was retained. The product has unique interconnected sub-micrometer sized macro-porous networks, and the walls of the interconnected 3D porous networks demonstrate a clear curved profile and a very low contrast, which arise from the ultrathin thickness and high mechanical flexibility (Fig. 2d).[34–39] If the sulfur precursor was replaced with L-cysteine (free of nitrogen functional group), some aggregated sub-micron particles with a diameter of about 200 nm on carbon sheets were clearly distinguished (Fig. S4b†). The morphology shown in Fig. 2d is significantly difference through use of L-cysteine, perhaps because of a linking role of nitrogen.[34–36] SEM images and XRD results of "bare Ni_3S_2" (prepared by adding NaCl but without citric acid) and "bulk Ni_3S_2/C" (obtained by adding citric acid as carbon precursors but without NaCl template) are also shown for comparison in Fig. S5.† Only large particles were obtained in bare Ni_3S_2, confirming that carbon can provide abundant surfaces and prevent Ni_3S_2 nanoparticles from agglomeration during the annealing process (Fig. S5a†). In Fig. S5b,† only Ni_3S_2 embedded in carbon layers could be attained. It should be emphasized that no coherent nanostructure was formed in bulk Ni_3S_2 + C products, demonstrating the key guidance role of the NaCl template. Results strongly indicate that the NaCl templates and carbon precursors play indispensable roles in formation of homogeneous coherent nanostructures. XRD results of coherent Ni_3S_2/C, bare Ni_3S_2, and bulk Ni_3S_2 + C (Fig. S5c†) show a pure phase of crystalline Ni_3S_2. The microstructures of the coherent Ni_3S_2/C were further studied by TEM, revealing a continuous ultrathin carbon layer anchored with uniform Ni_3S_2 nanoparticles (5–10 nm) (Fig. 2e). The carbon layers are about 5 nm in thickness, which facilitates rapid transport of electrons and sodium ions to Ni_3S_2 nanoparticles. Close examination under high-resolution TEM (Fig. 2f) reveals individual Ni_3S_2 nanocrystals with clear lattice fringes attached to carbon substrates.

TGA of coherent Ni_3S_2/C composites in air were recorded from room temperature to 700 °C. As shown in Fig. 3a, slight weight loss in the initial stage results from removal of water and residual organics. Approximately 73% of the original sample weight remained after TGA in air. The resultant solid combustion product is NiO (Fig. S6,† JCPDS: 47-1049). The overall reaction is given in eqn (2).

$$2Ni_3S_2 + 7O_2 \rightarrow 6NiO + 4SO_2 \quad (2)$$

The Ni_3S_2 content in the sample was estimated to be ~78.2%. The Raman spectrum (Fig. 3b) of the coherent Ni_3S_2/C composites presents two distinguishable peaks at 1351.7 cm^{-1} and 1591.7 cm^{-1}, which belong to the D-band and G-band of carbon, respectively. The D-band is related to the vibrations of carbon atoms with dangling bonds for the in-plane terminations of disordered graphite.[40] The G-band is the result of a C–C stretching mode of sp^2-bonded carbon.[41] In general, the intensity ratio between the D-band and G-band (I_D/I_G) provides a key

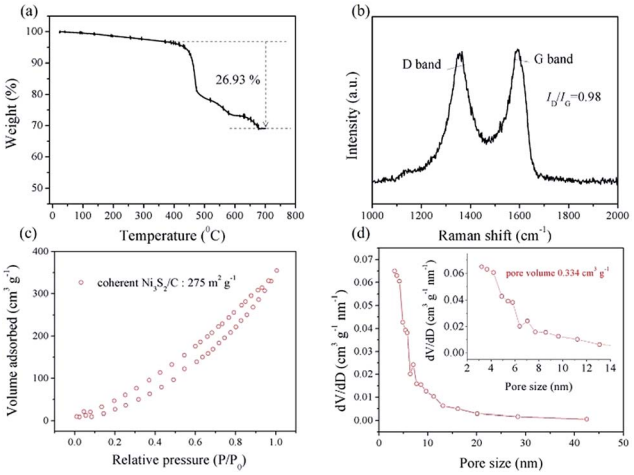

Fig. 3 (a) TGA result of coherent Ni_3S_2/C composite at temperatures ranging from 20 °C to 700 °C in air with a heating rate of 10 °C min^{-1}; (b) Raman spectrum of coherent Ni_3S_2/C composite showing typical D and G peaks with an identity ratio of 0.98; (c) nitrogen sorption isotherm of coherent Ni_3S_2/C composites, the BET surface area (275 $m^2 g^{-1}$) was determined using a multi-point-BET method; (d) pore size distribution of Ni_3S_2/C nanocomposite, the pore volume (0.334 $cm^3 g^{-1}$) was determined by a BJH-desorption method.

parameter for the graphitized degree of carbon materials. The I_D/I_G ratio of coherent Ni_3S_2/C is 0.98, which is beneficial for achieving high electrical conductivity. Well-graphitized carbon with high electrical conductivity may be very beneficial for fast electron transport. Fig. 3c shows the nitrogen isotherms of coherent Ni_3S_2/C composites. The hysteresis loops shown in isotherms of samples (type III) suggest the presence of macro-pores in the samples, consistent with the SEM results. The unique interconnected nanostructure shows a BET specific surface area of 275 $m^2 g^{-1}$, which is much higher than that of bulk Ni_3S_2 + C and bare Ni_3S_2 (as shown in Fig. S7a†). It also indicates that a broad pore size distribution of meso-pores (2–50 nm) with a pore volume of 0.334 $cm^3 g^{-1}$ can be attained (Fig. 3d), which is superior to those of bulk Ni_3S_2 + C and bare Ni_3S_2 (Fig. S7b and c†).

XPS analysis was conducted to study the elemental composition and chemical states of the coherent Ni_3S_2/C nanocomposite. As shown in Fig. 4a, the scanned C 1s spectrum can be deconvoluted into four peaks of C–C (284.4 eV, sp^2-hydridized carbon), C–N (285.3 eV), C–O (286.5 eV), and O–C=O (288.8 eV).[8,31] The oxygen can be derived from decomposition of oxygen-containing groups in citric acid during the pyrolysis process. In Fig. 4b, three forms of nitrogen, namely, graphitic N (400.5 eV), pyrrolic N (399.6 eV), and pyridinic N (398.2 eV) can be visualized. The presence of nitrogen is derived from decomposition of thiourea.[42] As observed, pyridinic N may be the dominant nitrogen species in Ni_3S_2/C nanocomposite. The presence of pyridinic nitrogen can increase electron conduction of the composite material by donation of the lone electron pair from N species to the graphitic carbon matrix, leading to improved rate property of the electrode.[42] In addition, the presence of N heteroatoms helps to enhance the whole architecture stability *via* the strong affinity of nanoparticles to the

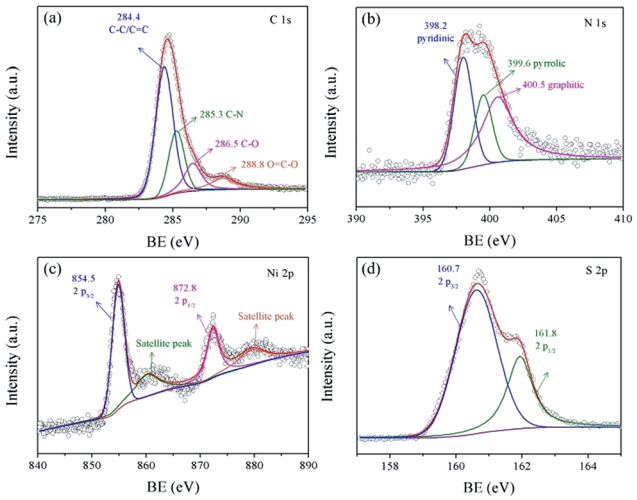

Fig. 4 High-resolution XPS spectra of (a) C 1s, (b) N 1s, (c) Ni 2p, and (d) S 2p of coherent Ni_3S_2/C nanocomposites.

carbon surface and the formation of defects for extra sodium storage.[23,24] In the Ni 2p XPS spectrum (Fig. 4c), the main peak at 854.5 eV can be assigned to Ni $2p_{3/2}$. The peak located at about 862 eV corresponds to the accompanied satellite peaks.[22–24,31–33] In the S 2p region (Fig. 4d), the peaks at 161.8 eV and 160.7 eV originate from S $2p_{1/2}$ and S $2p_{3/2}$ of S^{2-}. In general, the peaks in Ni 2p and S 2p spectra show obvious characteristics of Ni_3S_2, which consistent with the XRD and high resolution TEM results.[33]

3.2 Sodium ion storage performance

Fig. 5 illustrates the electrochemical properties of the resultant samples in Na-half cells. Fig. 5a displays the CV curves for the first three cycles of coherent Ni_3S_2/C nanocomposites at a scan rate of 0.2 mV s^{-1} in the voltage window of 0.01–3 V (*vs.* Na^+/Na). In the initial scan, a broad peak at about 0.43 V may be attributed to the conversion reaction and formation of the solid-electrolyte interphase (SEI) layer.[30–32] In the following cycles, this peak disappears and a couple of redox peaks can be observed at about 0.88/1.66 V, indicating the sodiation/desodiation of the electrode. Overlapping of CV curves in the second and third cycles indicates good electrode reversibility with reduced polarization after initial activation. The potential differences (ΔV) increase slightly (from 84 mV to 88 mV), indicating that reactions are highly reversible.[43] Fig. 5b shows the typical discharge/charge curves for coherent Ni_3S_2/C hybrids at a current density of 0.1 A g^{-1} between 0.01 and 3.0 V. Specifically, the initial discharge and charge capacities were 1012 and 598 mA h g^{-1}, respectively, with a coulombic efficiency (CE) of 59%. To examine whether the potential at which the SEI layer is believed to form corresponds with that in similar lithium electrolytes, the LIBs were assembled using similar solvent composition (home-made 1 M LiPF6 in EC/DEC/FEC, 1 : 1 : 0.05 in volume%). The corresponding CV curve is shown and discussed in Fig. S8.† The irreversible capacities of most transition metal sulfides (TMS) in Li or Na ion batteries are possibly caused by formation of the SEI layer and decomposition of electrolyte in the first cycle, which is common in many TMS-based anodes.[9,19,31,44] Also, the capacity loss of bare carbon was only 34% (Fig. S9†), which might cause the low CE in coherent Ni_3S_2/C electrode. The voltage platform hysteresis (about 0.3 V) in the first cycle may be caused by polarization of the anodes, possibly caused by a typical conversion reaction.[19,45,46] From the second cycle, the observed voltage plateaus are in accordance with the above CV results. In addition, the discharge and charge capacities in the second cycle were 656 and 590 mA h g^{-1}, respectively, corresponding to a higher CE of 90%. The CE was further increased to over 97% in the third cycle, suggesting good electrode reaction kinetics with high reversibility upon cycling. Fig. 5c shows the rate performance of the two samples as prepared, evaluated at various current densities from 0.1 to 2.0 A g^{-1}. Coherent Ni_3S_2/C composites showed a better rate performance overall than those of bulk Ni_3S_2 + C composites and bare Ni_3S_2. In the initial current density, the specific capacities showed a downwards trend mainly resulting from activation of anode materials. As the current densities increased from 0.1 to 0.2, 0.4, 0.8, 1.6, 2.0 A g^{-1}, the discharge capacities slightly decreased from 583 to 529, 491, 459, 421, 408 mA h g^{-1}, respectively, indicating superior rate capability of coherent Ni_3S_2/C composites. The specific capacity recovers 538 mA h g^{-1} after the current density is lowered to 0.1 A g^{-1}, with a retention rate of about 92%. The CE can be observed at over 99% after activating in the initial few cycles. Volumetric capacity was also roughly determined using whole anode volume (Fig. S10†). Low volumetric capacity might be caused by the loose packing of nanostructured materials. The bare carbon matrix was prepared by a similar route, with rate performance displayed in Fig. S11.† The low capacities of the single Ni_3S_2 and poor rate performance of the carbon matrix electrode indicate that the Ni_3S_2 and porous carbon networks could have a favorable synergistic effect that contributes to stabilizing reversible capacities and improving rate performances. In Fig. 5d, coherent Ni_3S_2/C nanocomposites deliver high and stable specific capacity of 453 and 431 mA h g^{-1} over 100 cycles with retention rates of 85% and 87% at 0.1 and 0.4 A g^{-1}, respectively. As seen from Fig. 5e, coherent Ni_3S_2/C nanocomposites possessed a reversible capacity of 427 mA h g^{-1} after three cycles of activation and only 4.4% capacity loss after 200 cycles, with the CE approaching 100%.

The preliminary results of the full-cell ($Na_3V_2(PO_4)_3$/rGO cathode || Ni_3S_2/C anode) demonstrate great potential for the as-prepared coherent Ni_3S_2/C to be used as an anode material in future SIBs. The choice of $Na_3V_2(PO_4)_3$ (named as NVP) cathode is mainly because of its high theoretical capacity and stable sodium super-ion conductor (NASICON) structure.[15,16] NVP/rGO was prepared *via* a sol–gel route (Fig. S12a†). Fig. S12b† shows the lamellar nanostructure with multi-stacked layers. Fig. S7c† shows a stable cyclic curve at 2C (1C $\approx$ 110 mA g^{-1}) for 100 cycles between 1.5 V and 4.0 V of NVP/rGO. The inset shows the NVP/rGO coupled flat charge and discharge plateaus at around 3.3 and 3.5 V, corresponding to the redox pair of V^{3+}/V^{4+}.[16] Fig. S13† highlights the composition and cycling performance of the full cell at a current density of 0.5 A g^{-1}. The full cell with

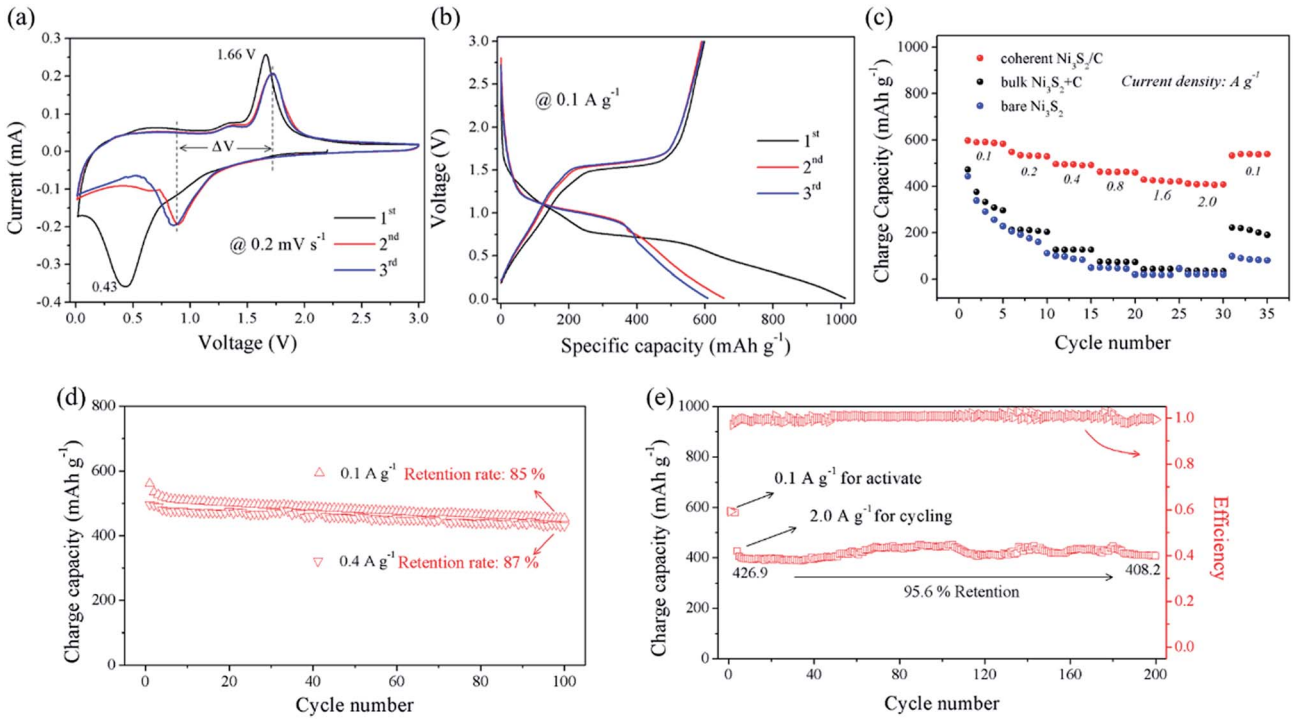

Fig. 5 (a) Cyclic voltammograms of coherent Ni_3S_2/C composites at a scan rate of 0.2 mV s^{-1} in the voltage window of 0.01–3 V (*vs.* Na^+/Na); (b) galvanostatic discharge–charge profiles of coherent Ni_3S_2/C composites for the first three cycles at a current density of 0.1 A g^{-1}; (c) rate charge capacities at various current densities from 0.1 to 2.0 A g^{-1}, then back to 0.1 A g^{-1}; (d) cyclic properties (100 cycles) at 0.1 and 0.4 A g^{-1} show stable cyclic performances with retention rates of 85% and 87%, respectively; (e) high density cyclic properties of coherent Ni_3S_2/C composites and coulombic efficiency at 2.0 A g^{-1}.

NVP (mass ratio between cathode and anode materials was 6 : 1) delivers an initial discharge capacity of 167 mA h g^{-1} at 0.5 A g^{-1} based on the mass of anode with an average discharge voltage platform of 1.7 V. The capacity was retained at 101 mA h g^{-1} after 30 cycles. In comparison with many similar anodes based on Ni_3S_2 (Table S1 in ESI†), the coherent Ni_3S_2/C electrode in this study exhibits much enhanced capacities and very attractive cycling stability at high rates.

3.3 Kinetics analyses

To further investigate the capacity–rate relationship in the coherent Ni_3S_2/C nanocomposites, the charge and discharge voltage profiles at various current densities are given in Fig. 6. Well defined, flat, and symmetric charge–discharge plateaus are clearly observed in Fig. 6a. When current densities increased, the charge and discharge plateaus were still clearly distinguishable. In contrast, bulk Ni_3S_2 + C and bare Ni_3S_2 show a rapid capacity drop when the current density is increased (Fig. 6b and c). The overpotential between charge and discharge voltage plateaus at various current densities further confirmed that the Ni_3S_2/C electrode possesses much less polarization and better reaction kinetics than of the bulk Ni_3S_2 + C and bare Ni_3S_2 electrodes (Fig. 6d), which can be attributed to the unique coherent structure inducing excellent electronic and ionic conductivity.[47]

Fig. 7a exhibits CV curves of coherent Ni_3S_2/C nanocomposite between 0.01 and 3.0 V at different scan rates. Two peaks are distinct in each curve at all scan rates. In cathodic scan, the peak shifts to a low potential area, while the peak shifts to a high potential area in anodic scan with increasing scan rate.[48] This is because redox reactions can occur over the

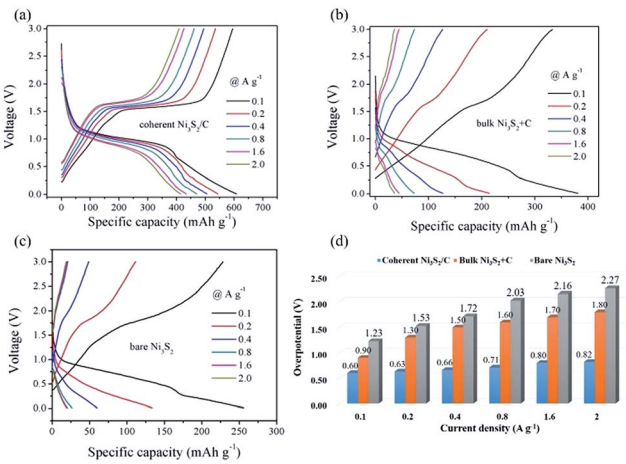

Fig. 6 Discharge–charge curves of (a) coherent Ni_3S_2/C nanocomposites, (b) bulk Ni_3S_2 + C composites, and (c) bare Ni_3S_2 at various current densities of 0.1, 0.2, 0.4, 0.8, 1.6, and 2.0 A g^{-1}; (d) calculated overpotentials based on the gaps of average voltages between charge and discharge voltage plateaus, indicating the merits of coherent structure for sodium ion and electron transportation with low overpotentials.

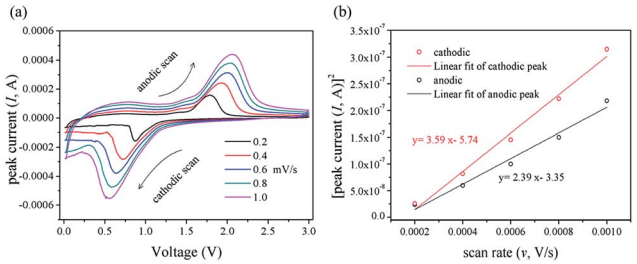

Fig. 7 (a) Cyclic voltammetry curves of the coherent Ni_3S_2/C electrode at different scan rates; (b) I^2 as a function of v for coherent Ni_3S_2/C electrode, indicating the diffusion coefficient (D) of coherent Ni_3S_2/C electrode is 1.3×10^{-12} cm^2 g^{-1} and 0.9×10^{-12} cm^2 g^{-1} for the cathodic peak and anodic peak, respectively.

entire active surface area while the scan rate is low; however, diffusion of sodium ions will be limited and the electrodes polarized at high scan rates. Therefore, only the outer active surface is effective for redox reactions, which results in position shift of both reduction and oxidation peaks.[14] Comparing Fig. 7 and S14,† there are clear redox peaks in the coherent Ni_3S_2/C nanocomposite with increasing scan rate to 1 mV s^{-1}, whereas the peaks become inconspicuous in the bulk Ni_3S_2 + C and bare Ni_3S_2 electrodes. Results demonstrate excellent reversibility and good electronic conductivity of the coherent Ni_3S_2/C electrodes. Based on the Randles–Sevchik equation for semi-infinite diffusion of sodium ions into electrodes, the apparent diffusion coefficients (D, cm^2 g^{-1}) were calculated according to eqn (3).[49]

$$D = \frac{I^2RT}{0.4463^2F^3N^3A^2C^2v} \quad (3)$$

where I (A) is peak current, R (8.314 J mol^{-1} K^{-1}) is gas constant, T (K) is the absolute temperature, F (96 485 C mol^{-1}) is the Faraday constant, N is the number of electrons transferred per molecule, A (cm^2) is the active surface area of the electrode, C (mol cm^{-3}) is the concentration of sodium ions in the electrolyte, and v (V s^{-1}) is the scanning rate. From the slope of the fitting line collected from oxidation and reduction peak current (I) (Fig. 7b), the diffusion coefficients D of the coherent Ni_3S_2/C electrode are 1.3×10^{-12} cm^2 g^{-1} and 0.9×10^{-12} cm^2 g^{-1} for the cathodic peak and anodic peak, respectively. The Na^+ diffusion coefficient of coherent Ni_3S_2/C nanocomposite is almost one magnitude larger than that of both bulk Ni_3S_2 + C and bare Ni_3S_2 electrodes (calculated in Fig. S14 in the ESI†), indicating that a coherent structure features much faster sodium ion diffusion. The electrochemical reaction kinetics of half-cells with coherent Ni_3S_2/C nanocomposite, bulk Ni_3S_2 + C and bare Ni_3S_2 were studied by electrochemical impendence spectroscopy (EIS). The measurements were carried out on the samples after 35 cycles under various rates. As shown in Fig. S15,† Nyquist plots of the three electrodes present depressed semicircles in the high frequency region and an inclined line in the low frequency range.[43,46] Coherent Ni_3S_2/C nanocomposite has much smaller charge transfer resistance and faster diffusion kinetics than of the bulk Ni_3S_2 + C and bare Ni_3S_2 samples, in agreement with the analysis in Fig. 7.

3.4 Electrochemical reaction mechanism

Ex situ XRD analyses of coherent Ni_3S_2/C anodes were performed at different stages in the first cycle, as shown in Fig. 8. The fresh anode shows a clear pattern of crystallized Ni_3S_2 (stage a). On discharge to 0.7 V (stage b), the Ni_3S_2 peaks disappear; a new peak located at about 37° emerges and can be assigned to Na_2S.[50] The main phase was Na_2S and no Ni_3S_2 phase can be observed, implying that the Ni_3S_2 lattice experienced a conversion reaction to Ni and Na_2S in the sodiation process. Although completing the discharge, the Na_2S peak was weak and no other obvious peaks were attained, suggesting that the discharge products were in amorphous states (stage c).[51] On desodiation to 1.7 V, a broad peak appeared belonging to Ni_3S_2 and the Na_2S was in an intensity reduction process, demonstrating the reversible reaction of the electrode. After charging to 3.0 V, the Ni_3S_2 reappeared but the peak intensity decreased, and Na_2S diminished (stage e). The broader peak and weaker peak intensity compared with the initial state indicate that the lattice expanded during the insert/extract of large sodium ions. Results reveal that sodium storage in our products is reversible. XRD patterns of bulk Ni_3S_2 + C and bare Ni_3S_2 in charge state (3.0 V) are shown in Fig. S9.† During the first cycle, both bulk Ni_3S_2 + C and bare Ni_3S_2 cannot return to their initial Ni_3S_2 phase. As certified in the literature,[10,14,17,19] most metal sulfides or selenides experience an insertion–conversion reaction during the first discharge process and can hardly return to their initial state when the charge process is completed. The by-products, known as poly-sulfides or poly-selenides, can experience shuttle and dissolving effects as in Li–S or Li–Se batteries, causing severe capacity loss. As shown in Fig. 8 and S16,† reactions in coherent Ni_3S_2/C are superiorly reversible to those of bulk Ni_3S_2 + C and bare Ni_3S_2. The coherent structures form an entangled network to confine the conversion reaction products in electrochemically active states, one possible explanation for the reversible reactions.

To evidence the effect of coherent networks on restrictions of poly-sulfides, cells were disassembled in a glove box after

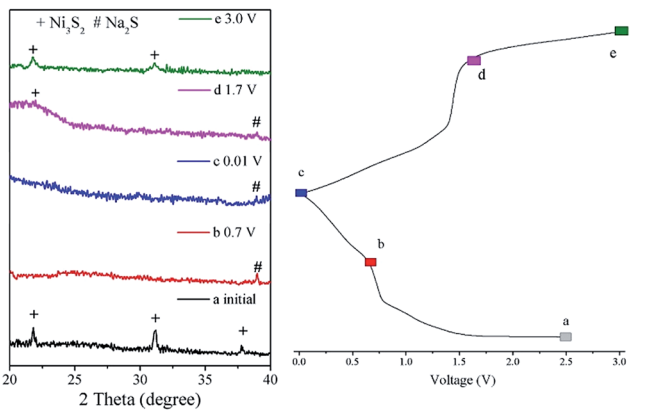

Fig. 8 *Ex situ* XRD patterns of the electrode collected at various points carried out under 100 mA g^{-1}, as indicated in the corresponding discharge/charge profiles: (a) pristine electrode, (b) after first discharge to 0.7 V, (c) after first discharge to 0.01 V, (d) after first charge to 1.7 V, and (e) after first charge to 3.0 V.

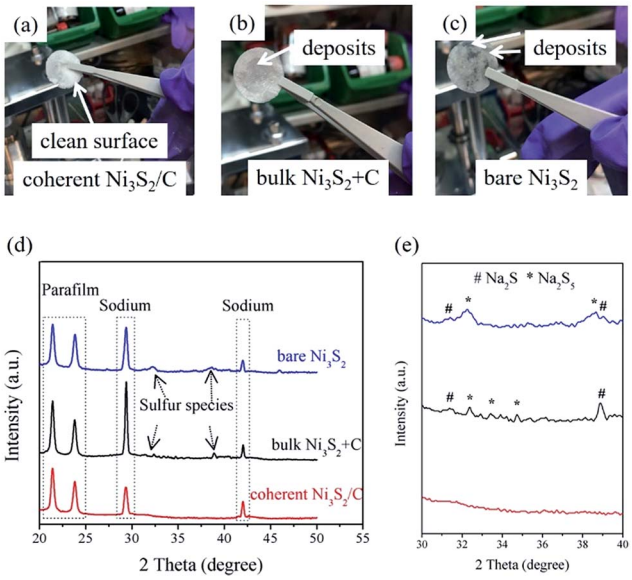

Fig. 9 Digital photos of separators from dissembled cells in glovebox: (a) coherent Ni_3S_2/C nanocomposites, (b) bulk Ni_3S_2 + C composites and (c) bare Ni_3S_2; (d) and (e) *ex situ* XRD patterns of the Na counter electrode after cycling collected from cells using coherent Ni_3S_2/C nanocomposites, bulk Ni_3S_2 + C composites, and bare Ni_3S_2 electrodes.

cycling under a low current density (Fig. S17†).[52] It is interesting to note that even after 20 cycles, some S species deposits were observed on the separator and Na anode for the "bulk Ni_3S_2 + C" and "bare Ni_3S_2" as shown by the digital images in Fig. 9a–c. In contrast, the membrane of the "coherent Ni_3S_2/C" electrode appeared clean and no obvious deposits could be observed. We also examined the Na counter electrodes after rate tests. After disassembly, the Na pieces were covered with parafilm to prevent possible surface oxidation and transferred immediately to a vacuum box (VWR® Container, the USA). Then, the XRD patterns were collected. As seen in Fig. 9d and e, in addition to some peaks assigned to parafilm and metal Na, some S species peaks could be identified on Na electrode when "bulk Ni_3S_2 + C" and "bare Ni_3S_2" electrodes were used.

4. Conclusions

Phase-purity coherent Ni_3S_2/C nanocomposites were successfully prepared *via* template-directed sol–gel processing and post-annealing. Nano-structural composites delivered superior sodium storage properties, exhibiting 453 and 430 mA h g^{-1} at a current density of 0.1 and 0.4 A g^{-1} over 100 cycles, respectively. Even at a high current density of 2.0 A g^{-1}, only 4.4% capacity loss was observed after 200 cycles. The reaction mechanism of the as-prepared electrodes was investigated, demonstrating reversible conversion processes in the sodiation/desodiation reactions. The outstanding cyclic and rate behaviors and enhanced Na^+ diffusion abilities, as well as superior reversibility, can be attributed to the unique structure. The novel coherent architectures afford an efficient electrode/electrolyte contact interface and enough active sites for sodium ion insertion/extraction, resulting in fast reaction kinetics. More importantly, the entangled networks in coherent Ni_3S_2/C nanocomposites can confine the discharge products, providing long-term cycling stability. $Na_3V_2(PO_4)_3$/Ni_3S_2 full cells with high performances are promising in development of commercial SIBs using Earth-abundant transition metal sulfide anodes.

Acknowledgements

This work was supported by the National Natural Science Foundation of China (no. 51622101 and 51471061), National Natural Science (DMR no. 1505902). Dr Xu Zhao (no. 201506120144) and Dr Hong-En Wang (no. 201506955047) gratefully acknowledge the financial support from the China Scholarship Council (CSC) during their study in University of Washington, Seattle. Dr Hong-En Wang also acknowledges Hubei Provincial Department of Education for the "Chutian Scholar" program. Part of this work was conducted at the Molecular Analysis Facility, a National Nanotechnology Coordinated Infrastructure site at the University of Washington, which is supported by the National Science Foundation (grant ECC-1542101) and the Clean Energy Institute.

References

1 M. Armand and J. M. Tarascon, *Nature*, 2008, **451**, 652.
2 C. F. Liu, R. C. Masse, X. H. Nan and G. Z. Cao, *Energy Storage Materials*, 2016, **4**, 15.
3 R. C. Massé, C. F. Liu, Y. W. Li, L. Q. Mai and G. Z. Cao, *Natl. Sci. Rev.*, 2017, **4**, 26; R. Masse, E. Uchaker and G. Z. Cao, *Sci. China Mater.*, 2015, **58**, 715.
4 J. B. Goodenough and K. S. Park, *J. Am. Chem. Soc.*, 2013, **135**, 1167.
5 (*a*) J. H. Sui, J. Li, J. Q. He, Y. L. Pei, D. Berardan, H. J. Wu, N. Dragoe, W. Cai and L. D. Zhao, *Energy Environ. Sci.*, 2013, **6**, 2916; (*b*) Z. H. Liu, Y. M. Wang, J. Mao, H. Y. Geng, J. Shuai, Y. X. Wang, R. He, W. Cai, J. H. Sui and Z. F. Ren, *Adv. Energy Mater.*, 2016, **6**, 1502269.
6 J. Ding, H. Zhou, H. L. Zhang, T. Stephenson, Z. Li, D. Karpuzov and D. Mitlin, *Energy Environ. Sci.*, 2017, **10**, 153.
7 D. Larcher and J. M. Tarascon, *Nat. Chem.*, 2015, **7**, 19.
8 Y. Jiang, M. Wei, J. K. Feng, Y. C. Ma and S. L. Xiong, *Energy Environ. Sci.*, 2016, **9**, 1430.
9 B. H. Qu, C. Z. Ma, G. Ji, C. H. Xu, J. Xu, Y. S. Meng, T. H. Wang and J. Y. Lee, *Adv. Mater.*, 2014, **26**, 3854.
10 D. Xie, X. H. Xia, Y. Zhong, Y. D. Wang, D. H. Wang, X. L. Wang and J. P. Tu, *Adv. Energy Mater.*, 2017, **7**, 1601804.
11 (*a*) D. L. Chao, C. Zhu, P. Yang, X. H. Xia, J. Liu, J. Wang, X. Fan, S. V. Savilov, J. Lin, H. J. Fan and Z. X. Shen, *Nat. Commun.*, 2016, **7**, 12122; (*b*) D. L. Chao, P. Liang, Z. Chen, L. Y. Bai, H. Shen, X. X. Liu, X. H. Xia, Y. L. Zhao, S. V. Savilov, J. Y. Lin and Z. X. Shen, *ACS Nano*, 2016, **10**, 10211.
12 (*a*) Z. Hu, Z. Q. Zhu, F. Y. Cheng, K. Zhang, J. B. Wang, C. C. Chen and J. Chen, *Energy Environ. Sci.*, 2015, **8**, 1309; (*b*) K. Zhang, M. H. Park, L. M. Zhou, G.-H. Lee, W. J. Li, Y. M. Kang and J. Chen, *Adv. Funct. Mater.*, 2016, **26**, 6728;

(*c*) K. Zhang, M. H. Park, L. M. Zhou, G.-H. Lee, J. Shin, Z. Hu, S.-L. Chou, J. Chen and Y. K. Kang, *Angew. Chem., Int. Ed.*, 2016, **55**, 12822; (*d*) Z. Hu, L. X. Wang, K. Zhang, J. B. Wang, F. Y. Cheng, Z. L. Tao and J. Chen, *Angew. Chem., Int. Ed.*, 2014, **53**, 13008.

13 C. Wu, Y. Jiang, P. Kopold, P. A. Aken, J. Maier and Y. Yu, *Adv. Mater.*, 2016, **28**, 7276.

14 F. Zhang, C. Xia, J. J. Zhu, B. Ahmed, H. F. Liang, D. B. Velusamy, U. Schwingenschlögl and H. N. Alshareef, *Adv. Energy Mater.*, 2016, **6**, 1601188.

15 W. H. Ren, Z. P. Zheng, C. Xu, C. J. Niu, Q. L. Wei, Q. Y. An, K. N. Zhao, M. Y. Yan, M. S. Qin and L. Q. Mai, *Nano Energy*, 2016, **25**, 145.

16 Y. N. Xu, Q. L. Wei, C. Xu, Q. D. Li, Q. Y. An, P. F. Zhang, J. Z. Sheng, L. Zhou and L. Q. Mai, *Adv. Energy Mater.*, 2016, **6**, 1600389.

17 C. George, A. J. Morris, M. H. Modarres and M. D. Volder, *Chem. Mater.*, 2016, **28**, 7304.

18 (*a*) Y. Xiao, S. Lee and Y. K. Sun, *Adv. Energy Mater.*, 2017, **7**, 1601329; (*b*) C. F. Liu, C. K. Zhang, H. Y. Fu, X. H. Nan and G. Z. Cao, *Adv. Energy Mater.*, 2017, **7**, 1601127.

19 X. M. Li, J. T. Zai, S. J. Xiang, Y. Y. Liu, X. B. He, Z. Y. Xu, K. X. Wang, Z. F. Ma and X. F. Qian, *Adv. Energy Mater.*, 2016, **6**, 1601056.

20 Y. P. Liu, H. T. Wang, L. Cheng, N. Han, F. P. Zhao, P. R. Li, C. H. Jin and Y. G. Li, *Nano Energy*, 2016, **20**, 168.

21 W. C. Duan, W. C. Yan, X. Yan, H. Munakata, Y. C. Jin and K. Kanamura, *J. Power Sources*, 2015, **293**, 706–711.

22 W. Zhou, J. L. Zheng, Y. H. Yue and L. Guo, *Nano Energy*, 2015, **11**, 428–435.

23 D. Li, X. W. Li, X. Y. Hou, X. L. Sun, B. L. Liu and D. Y. He, *Chem. Commun.*, 2014, **50**, 9361.

24 J. L. Zhu, Y. Y. Li, S. Kang, X.-L. Wei and P. K. Shen, *J. Mater. Chem. A*, 2014, **2**, 3142.

25 T. Zhu, H. B. Wu, Y. B. Wang, R. Xu and X. W. Lou, *Adv. Energy Mater.*, 2012, **2**, 1497.

26 L.-L. Feng, G. T. Yu, Y. Y. Wu, G.-D. Li, H. Li, Y. H. Sun, T. Asefa, W. Chen and X. X. Zou, *J. Am. Chem. Soc.*, 2015, **137**, 14023.

27 R. Li, S. L. Wang, J. P. Wang and Z. C. Huang, *Phys. Chem. Chem. Phys.*, 2015, **17**, 16434.

28 J.-S. Kim, H.-J. Ahn, H.-S. Ryu, D.-J. Kim, G.-B. Cho, K.-W. Kim, T.-H. Nam and J. H. Ahn, *J. Power Sources*, 2008, **178**, 852.

29 P. A. Metcalf, P. Fanwick, Z. Kąkol and J. M. Honig, *J. Solid State Chem.*, 1993, **104**, 81.

30 C. Q. Shang, S. M. Dong, S. L. Zhang, P. Hu, C. J. Zhang and G. L. Cui, *Electrochem. Commun.*, 2015, **50**, 24.

31 F. P. Zhao, Q. F. Gong, B. Traynor, D. Zhang, J. J. Li, H. L. Ye, F. J. Chen, N. Han, Y. Y. Wang, X. H. Sun and Y. G. Li, *Nano Res.*, 2016, **302**, 3162.

32 W. Qin, T. Q. Chen, T. Lu, D. H. Chua and L. K. Pan, *J. Power Sources*, 2016, **302**, 202–209.

33 X. S. Song, X. F. Li, Z. M. Bai, B. Yan, D. J. Li and X. L. Sun, *Nano Energy*, 2016, **26**, 533–540.

34 J. Qin, C. N. He, N. Q. Zhao, Z. Y. Wang, C. S. Shi, E.-Z. Liu and J. J. Li, *ACS Nano*, 2014, **8**, 1728.

35 C. N. He, S. Wu, N. Q. Zhao, C. Shi, E.-Z. Liu and J. J. Li, *ACS Nano*, 2013, **7**, 4459.

36 J. Zhou, J. Qin, X. Zhang, C. S. Shi, E.-Z. Liu, J. J. Li, N. Q. Zhao and C. N. He, *ACS Nano*, 2015, **9**, 3837.

37 W. Y. Li, Y. B. Tang, W. P. Kang, Z. Y. Zhang, X. Yang, Y. Zhu, W. J. Zhang and C. S. Lee, *Small*, 2015, **11**, 1345.

38 S. Zhu, J. J. Li, L. Y. Ma, L. C. Guo, Q. Y. Li, C. N. He, E.-Z. Liu, F. He, C. S. Shi and N. Q. Zhao, *ACS Appl. Mater. Interfaces*, 2016, **8**, 11720.

39 X. J. Liu, J. T. Zai, B. Li, J. Zou, Z. F. Ma and X. F. Qian, *J. Mater. Chem. A*, 2016, **4**, 10552.

40 Y. Zheng, T. F. Zhou, C. F. Zhang, J. F. Mao, H. K. Liu and Z. P. Guo, *Angew. Chem., Int. Ed.*, 2016, **55**, 3408.

41 H. Jiang, D. Y. Ren, H. F. Wang, Y. J. Hu, S. J. Guo, H. Y. Yuan, P. J. Hu, L. Zhang and C. Z. Li, *Adv. Mater.*, 2015, **27**, 3687.

42 (*a*) M. B. Li, H. H. Zhou, W. J. Yang, L. Chen, Z. Huang, N. S. Zhang, C. P. Fu and Y. F. Kuang, *J. Mater. Chem. A*, 2017, **5**, 1014; (*b*) G. J. He, M. Qiao, W. Y. Li, Y. Lu, T. T. Zhao, R. J. Zou, B. Li, J. A. Darr, J. Hu, M. M. Titirici and I. P. Parkin, *Adv. Sci.*, 2017, **4**, 1600214.

43 X. Zhao, J. H. Sui, F. Li, H.-T. Fang, H. E. Wang, J. Y. Li, W. Cai and G. Z. Cao, *Nanoscale*, 2016, **8**, 17902.

44 D. Zhang, W. Sun, Y. Zhang, Y. H. Dou, Y. Z. Jiang and S. X. Dou, *Adv. Funct. Mater.*, 2016, **26**, 7479–7485.

45 L. David, R. Bhandavat, U. Barrera and G. Singh, *Sci. Rep.*, 2015, **5**, 9792.

46 Q. Zhou, L. Liu, Z. Huang, L. Yi, X. Wang and G. Z. Cao, *J. Mater. Chem. A*, 2016, **4**, 5505.

47 Z. Li, J. Zhang, B. Guan, D. Wang, L. Liu and X. W. Lou, *Nat. Commun.*, 2016, **7**, 13065.

48 C. K. Zhang, H. Q. Song, C. F. Liu, Y. G. Liu, C. P. Zhang, X. H. Nan and G. Z. Cao, *Adv. Funct. Mater.*, 2015, **25**, 3497.

49 A. J. Bard and L. R. Faulkner, *Electrochemical Methods: Fundamentals and Applications*, Wiley, New York 1980, p. 213.

50 W. P. Sun, X. H. Rui, D. Yang, Z. Q. Sun, B. Li, W. Y. Zhang, Y. Zong, S. Madhavi, S. X. Dou and Q. Y. Yan, *ACS Nano*, 2015, **9**, 11371.

51 T. F. Zhou, W. K. Pang, C. F. Zhang, J. P. Yang, Z. X. Chen, H. K. Liu and Z. P. Guo, *ACS Nano*, 2014, **8**, 8323.

52 W.-H. Ryu, H. Wilson, S. Sohn, J. Y. Li, X. Tong, E. Shaulsky, J. Schroers, M. Elimelech and A. D. Taylor, *ACS Nano*, 2016, **10**, 3257; W. H. Ryu, J. W. Jung, K. Park, S. J. Kim and I. D. Kim, *Nanoscale*, 2014, **6**, 10975.

